





Article

Enhancing the Thermal Performance of Slender Packed Beds through Internal Heat Fins

Nico Jurtz ^{1,*} , Steffen Fleischlen ² , Sören C. Scherf ², Matthias Kraume ¹ 
and Gregor D. Wehinger ² 

¹ Chair of Chemical and Process Engineering, Technische Universität Berlin, Ackerstr. 76, 13355 Berlin, Germany; matthias.kraume@tu-berlin.de

² Institute of Chemical and Electrochemical Process Engineering, Clausthal University of Technology, Leibnizstr. 17, 38678 Clausthal-Zellerfeld, Germany; flaischlen@icvt.tu-clausthal.de (S.F.); soeren.scherf@tu-clausthal.de (S.C.S.); wehinger@icvt.tu-clausthal.de (G.D.W.)

* Correspondence: nico.jurtz@tu-berlin.de; Tel.: +49-30-314-70078

Received: 7 October 2020; Accepted: 18 November 2020; Published: 24 November 2020



Abstract: Slender packed beds are widely used in the chemical and process industry for heterogeneous catalytic reactions in tube-bundle reactors. Under safety and reaction engineering aspects, good radial heat transfer is of outstanding importance. However, because of local wall effects, the radial heat transport in the vicinity of the reactor wall is hindered. Particle-resolved computational fluid dynamics (CFD) is used to investigate the impact of internal heat fins on the near wall radial heat transport in slender packed beds filled with spherical particles. The simulation results are validated against experimental measurements in terms of particle count and pressure drop. The simulation results show that internal heat fins increase the conductive portion of the radial heat transport close to the reactor wall, leading to an overall increased thermal performance of the system. In a wide flow range ($100 < Re_p < 1000$), an increase of up to 35% in wall heat transfer coefficient and almost 90% in effective radial thermal conductivity is observed, respectively.

Keywords: packed bed reactor; heat transfer; pressure drop; process intensification; heat fins; computational fluid dynamics (CFD); Discrete Element Method (DEM)

1. Introduction

Multitubular packed bed reactors are widely used in the chemical and process industry for highly endothermic or exothermic catalytic reactions. They consist of up to thousands of tubes filled with catalyst particles, whereby a heat transfer media, e.g., a molten salt or gas heated by combustion, is circulated around the tubes to either provide or remove the heat of reaction. To ensure an adequate radial heat transfer within the reactor tubes, the tube diameter is usually very low (2–8 cm) [1]. On the other hand, the pressure drop needs to be kept low, that is why relatively large particles are used, which leads to slender packed beds characterized by a low tube-to-particle diameter ratio N .

For this reactor configuration the assumption of a homogeneously distributed void fraction does not hold true, as the confining walls exert an ordering effect on the particle structure. This leads to a radial void fraction distribution that is characterized by several distinct minima and maxima, as exemplary shown in Figure 1 for spheres. Directly at the wall, only a point contact exists between particles and the tube wall, leading to a bed voidage of $\epsilon = 1$. Because of the ordering wall effect, particles tend to build a

layer close to the wall. This leads to a global minimum in bed voidage at a distance of half a sphere away from the wall. After a distance of one particle diameter, the first layer of particles ends, leading to a global maximum in bed voidage. With increasing distance from the wall the ordering effect gets more and more lost, leading to a damped oscillatory progression of the radial void fraction distribution. The unevenly distributed bed voidage significantly impacts the fluid dynamics in the bed structure as it can be seen in Figure 1 in terms of the radial profile of the average axial velocity normalized by the superficial velocity. The radial velocity profile corresponds to the radial void fraction distribution and shows an increased axial velocity at positions where the bed voidage is high, which is because the flow tends to take the path of the lowest resistance. Close to the reactor wall a global maximum in axial velocity can be seen which is known as the wall channeling effect. It is widely accepted that this effect negatively influences the radial heat transport close to the wall, and, therefore, limits the thermal performance of the overall system. According to Yagi and Kunii [2], the reduced heat transfer can be attributed to three different effects, which are: (1) the reduced solid conductivity close to the wall as a result of increased voidage, (2) the buildup of a laminar boundary layer at the wall, and (3) a reduced lateral convective mixing.

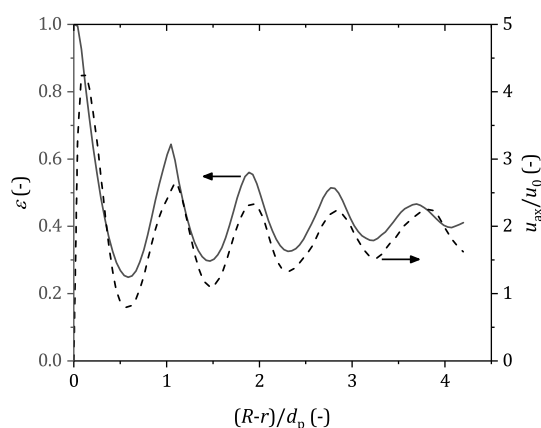


Figure 1. CFD simulation result of the radial void fraction distribution and radial profile of the averaged normalized axial velocity for a packing of spherical particles ($N = 8.8$).

Recently, several research groups have addressed this topic, investigating reactor concepts to increase the radial heat transfer in gas-solid systems. Some of those concepts are shown illustratively in Figure 2. The main research focus is on the investigation of the impact of particle shape on fluid dynamics, heat/mass transfer and chemical conversion. The experimental work of Giese et al. [3] showed that the use of Raschig rings or deformed spheres lead to a more homogeneous radial void fraction distribution and less radial variance in axial velocity in the inner region of the packed bed. However, it was also shown that the wall channeling as such could not fully be avoided. This finding was later verified by the numerical work of Caulkin et al. [4] and Wehinger et al. [5]. The former of both authors showed that even for trilobes, although characterized by an almost homogeneous void fraction profile, a wall channeling effect occur, caused by the steep increase of bed voidage close to the wall. Nevertheless, although the wall channeling cannot totally be avoided by the choice of complex particle shapes, it can be at least reduced. Martin and Nilles [6] demonstrated, that compared to spheres, Raschig rings show a higher wall heat transfer coefficient over a large Reynolds number range. However, the authors also highlighted that cylinder packings show a slightly higher heat transfer coefficient, although the tendency for wall channeling is higher compared to rings. A possible explanation for this is the higher conductive resistance of rings caused by the lower amount of solid material in the system. Although, from a fluid dynamic point of view, complex particle shapes may not solve entirely the radial heat transfer

problem, from a reaction engineering point of view, it offers many possibilities as recently shown [5,7,8]. Especially, different catalyst suppliers present very different types of shapes for different applications, e.g., wagon wheels, toothed wheels, flute wheels, daisy-types, tri- or multi-lobes, stars, and many more [9,10].

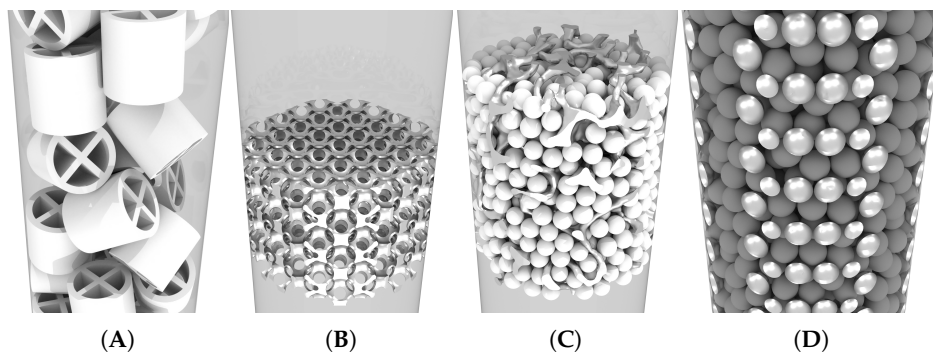


Figure 2. Recent process intensification concepts for catalytic flow reactors: (A) Complex particle shapes, (B) Periodic open cell structures, (C) Packed foams and (D) Macroscopic wall structures.

An alternative concept to overcome the radial heat transfer problem in catalytic flow reactors represent periodic open cell structures (POCS), as proposed by the research groups at FAU Erlangen-Nuremberg [11–13] and visualized in Figure 2B. This concept combines the beneficial characteristics of honeycomb monoliths, e.g., low pressure drop and high thermal conductivity, with the high radial mass transfer of open-cell foams. The packings are based on unit cells, e.g., cubic, diamond or tetradecahedron cells, which are arranged periodically and repetitively. POCS are proposed as alternatives to random bed structures or honeycombs in gas-solid or gas-liquid-solid applications [11–13]. The latter authors investigated the impact of material, morphology and wall coupling on the thermal performance of POCS. The material, and likewise the solid thermal conductivity, only affected the stagnant part of the effective radial thermal conductivity of the system, leading to a parallel shift of the effective radial thermal conductivity for different materials plotted over superficial gas velocity. The authors found that an increasing voidage leads to a reduced stagnant conductivity, while with decreasing cell density the effective radial thermal conductivity increases faster, if the superficial gas velocity is raised. This reveals one drawback of the concept: Although the specific surface area with respect to the reactor volume is high ($a_v \approx 400\text{--}800\text{ m}^{-1}$), the absolute available surface area is limited, because the voidage is usually also high ($\varepsilon = 0.8\text{--}0.95$), and a high cell density (number of void cells per inch) has a negative effect on the effective radial thermal conductivity. The wall coupling seems not to be too critical, as it was found that 10–20% wall coupling is sufficient for an effective wall heat transfer. However, it was shown that in comparison to conventional packed bed reactors with the same specific surface area, POCS are only beneficial for low to moderate superficial velocities of $v_0 \leq 1.8\text{ m/s}$, which corresponds to a maximum Particle Reynolds number of $Re_p \approx 350$. This could limit the throughput under optimal operating conditions and thus leads to larger reactor dimensions, resulting in higher investment costs. Furthermore, there may be limitations on the manufacturability of large scale POCS.

Also inspired by the superior heat transfer characteristic of open-cell foams is the packed foams reactor concept proposed by Ambrosetti et al. [14] (see schematically Figure 2C) and the packed-POCS concept by Fratolocchi et al. [15] and Ambrosetti et al. [16]. Here, the open-cell foam or POCS are just a carrier to enhance the heat transfer. The catalytic active surface area is provided by traditional pellets that are poured into the reactor and fill the interstices. In their numerical and experimental study, Ambrosetti et al. [14,16] found that the packing efficiency ($V_{p,\text{total}} / (V_{\text{total}} - V_{\text{POCS}})$) is mainly affected by the pore-to-pellet size

ratio. For a ratio of $d_{\text{pore}}/d_p \geq 3$ the bed voidage approaches asymptotically the value of conventional packed beds filled with the same type of particles. Furthermore, the authors found that the specific pressure drop of packed foams is in the same order of magnitude as for a packed bed, if the foam has a high void fraction ($\varepsilon_{\text{foam}} = 0.9$). This becomes significantly higher, if the foam voidage decreases. For the reactor design, this results in a trade-off between good thermal conductivity and low pressure drop. Since the foam structure occupies space that is not available for catalyst particles, this leads in an overall higher pressure drop per active catalyst surface area in comparison to conventional packed beds. However, it was shown by Fratalocchi et al. [15] that for Fischer-Tropsch synthesis, the packed foam concept leads to almost isothermal reaction conditions and higher conversion in comparison to conventional packed beds. In comparison to packed foams, packed-POCS show an increased bulk heat transfer characteristic and wall heat transfer, respectively.

A completely different concept to solve the radial heat transfer problem in packed beds is proposed by Zobel et al. [17] and Eppinger et al. [18], see Figure 2D. They suggest macroscopic wall structures to disturb the regular particle arrangement close to the wall. With that, they achieved a more homogeneous axial and radial void fraction distribution, leading to a more plug-flow-like flow characteristic. Zobel et al. [17] demonstrated, that, close to the wall, lateral mixing is significantly increased, showing an average radial velocity of up to 30% higher, compared to the case without wall structures. In their numerical study, Eppinger et al. [18] noticed an up to 40% increase in lateral mixing when using appropriate macroscopic wall structures. They also found that the wall channeling effect can totally be avoided by using specific wall structures, e.g., randomly arranged spherical caps. The concept itself is interesting, because it directly addresses the underlying mechanisms of the radial heat transport problem without changing the reactor type too much. One potential drawback is the manufacturability of the specific designs for these wall structures, which depends on the utilized pellet shape and size.

Comparing the different concepts discussed above, one can distinguish between two different mechanisms to increase the radial heat transfer: One can either increase the radial conductive heat transfer, as in the case of POCS and packed foams, or one increases the convective lateral mixing close to the wall, which can be achieved by macroscopic wall structures. A traditional approach to increase the heat transfer from a surface to a surrounding fluid is the use of pin-fins in a wide variety of engineering applications, e.g., cooling of turbine airfoils, electronics, etc. [19–21]. In the field of packed bed reactors, however, this is not commonly used, and, therefore, only limited work has previously been conducted in that field. Nakaso et al. [22] investigated the impact of shell-side fins on the thermal performance of a tube-side heated packed bed and found an up to thirty times higher effective thermal conductivity if spiral-type heat fins are used. The impact of pin-fin heat sinks on the heat transfer in packings of spherical particles were investigated by Jeng et al. [23], and a significant increase in the Nusselt number was observed, comparing a bottom heated cubic packing of spherical brass particles with heat fins against the configuration without them. The impact of fins in adsorption cooling units was investigated by numerous authors, e.g., [24,25], showing beneficial characteristics of heat fins for this kind of application.

To the best of our knowledge, the impact of internal heat fins on the heat transfer inside cylindrical packed bed reactors has not been investigated by now. The basic idea is to bridge the near wall region, that is characterized by low lateral mixing and thermal conductivity, using fins made of highly conductive material. This is similar to the mechanism that leads to the beneficial thermal behavior of open-cell foams or POCS, however, only limited to the region close to the reactor wall, and without changing the general characteristics of a packed bed too much. If a positive effect of internal heat fins can be found, this would offer the possibility of equipping new and already existing units with that device, since the heat fins could be manufactured, for example as a sleeve, that can be inserted into the reactor tubes.

In the first part of this study, details are given about the additive manufacturing process used to produce a helical finned sleeve. Filling experiments are conducted and numerically replicated, using the

Discrete Element Method (DEM), to investigate the impact of heat fins on the bed voidage, and with that, the specific surface area of the catalyst particles. In the next part, the impact of the heat fins on the pressure drop is investigated experimentally and numerically, followed by a numerical study examining the impact of internal heat fins on the fluid dynamics and heat transfer. This study is limited to spherical particles. However, other particle shapes of fin shapes and/or dimensions might have an even larger positive effect on the reactor performance.

2. Materials and Methods

In the scope of this work, we investigate the fluid dynamics and heat transfer packed beds made of spherical particles with a diameter of $d_p = 7$ mm that are filled in a cylindrical container with a nominal diameter of $D = 25.4$ mm. The study is divided into two separate parts. First, the manufacturability using 3D printing is tested by producing helical fin sleeve modules. As this part of the study is limited to fluid dynamic investigations only, and, therefore, the thermal conductivity of the fins does not play a role, Polylactid (PLA) filaments are used. The sleeves are plugged into the reactor tube that is subsequently filled with spherical particles and the particle count is determined. The pressure drop of the reactor without heat fins is compared against the one of the reactor with helical fins. The experimental results are compared with simulation results to validate the numerical model.

In the second part, the impact of different fin designs on the heat transfer is investigated numerically. Two different types of heat fins are tested and compared against the reference case without internals. Here, it is assumed that the heat fins are made of stainless steel, a material that can also be used in additive manufacturing processes, but has a significantly higher thermal conductivity in comparison to PLA. The reactor is heated by applying a constant wall temperature of 200 °C.

All investigated fins have a material thickness of 1.0 mm and a nominal width of 4.2 mm. The helical design has a pitch of 120 mm. Two fins are arranged opposite each other. Figure 3 provides an overview of the investigated designs, showing the empty and filled reactor. For all investigated packings the bed height is $H = 600$ mm, whereas rather dense packings were created in the experiments, which was accounted for in the numerical filling simulation by lowering the static friction coefficient to 0.01 as proposed by Jurtz et al. [10,26]. All relevant properties and boundary conditions are summarized in Table 1.

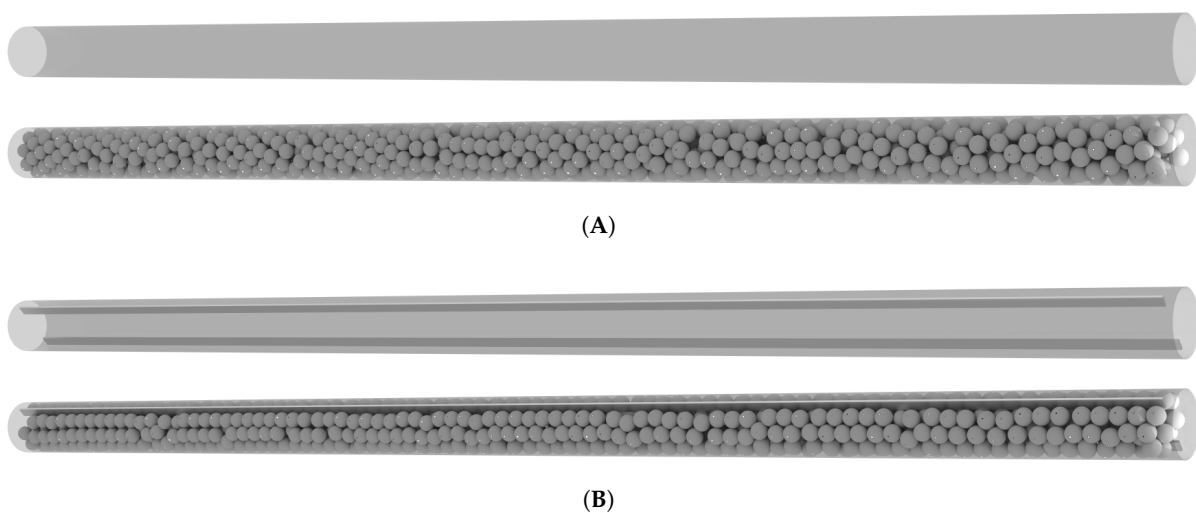


Figure 3. Cont.

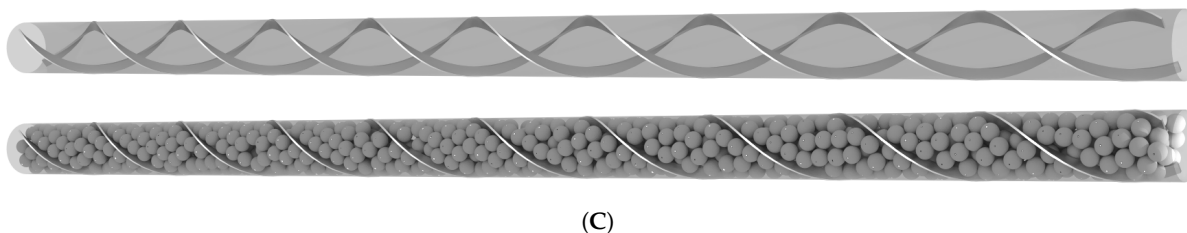


Figure 3. Visualization of the investigated reactor designs: Tube without heat fins (A), with straight heat fins (B), and with helical heat fins (C). Tube diameter = 25.4 mm; particle diameter = 7 mm; fin depth = 4.2 mm; fin thickness = 1 mm.

Table 1. Properties and boundary conditions used.

Fluid Dynamic Validation Study:	
Inlet velocity [m/s] (without fins)	0.21; 0.41; 0.76; 1.04; 1.25; 1.46; 1.58
Inlet velocity [m/s] (helical fins)	0.21; 0.41; 0.77; 1.05; 1.26; 1.47; 1.54
Numerical Heat Transfer Study:	
Inlet velocity [m/s]	0.22; 1.10; 2.20
Inlet temperature [°C]	20
Wall temperature [°C]	200
Thermal conductivity of particles [W/(m K)]	0.25
Thermal conductivity of heat fins [W/(m K)]	15.10
Thermal conductivity of gas phase [W/(m K)]	0.026

2.1. Experimental Methods

The demands on production of the heat fins are comparatively high, since the filigree double helix is very thin and the outer diameter of the geometry is comparatively small. Conventional manufacturing, e.g., forming from a metal profile, is possible in principle, but requires a corresponding forming tool, high technical know-how and, due to the necessary precision, manual skills. With the help of 3D printing (additive manufacturing), it is possible to produce complex geometries fully automatically on the basis of a CAD design. In principle, polymers and metals are processed layer by layer. The starting materials are applied e.g., as filament, liquid or powder and solidified by an activation source according to the material. An overview about 3D printing in chemical engineering is given by Parra-Cabrera et al. [27].

2.1.1. Additive Manufacturing Process

For the experimental investigation of the pressure loss, functional prototypes of the heat fins were produced. To achieve good results, a 3D printing process needs to be able to produce the complex geometry with the appropriate precision and sufficiently high mechanical strength. To meet these requirements, two cost-effective 3D printing processes for the so called rapid prototyping (3D printing and experimental) were tested: stereolithography and fused layer modeling (FLM). The stereolithography process uses a laser to solidify a liquid resin layer by layer [28]. In FLM, a polymer filament is melted in an extruder and selectively deposited layer by layer to produce three-dimensional components [29].

The filigree double helix geometry requires the use of support material to enable a reliable additive manufacturing process. In the FLM process, these support structures made of water-soluble Polyvinyl alcohol (PVA) material can be processed automatically with an additional nozzle and removed easily in an ultrasonic bath. We, therefore, decided to use the FLM *Ultimaker 3* system from *Ultimaker* with an extruder die diameter of 0.25 mm, PLA filament and PVA support material. Due to the limited building space of the *Ultimaker 3*, we divided the heat fin (600 mm total height) into four parts of equal length and added

support rings to the CAD model. These rings support the shape accuracy of the individual elements and also ensure correct orientation of the four parts during assembly, as well as when filling the tube with pellets (see Figure 4).

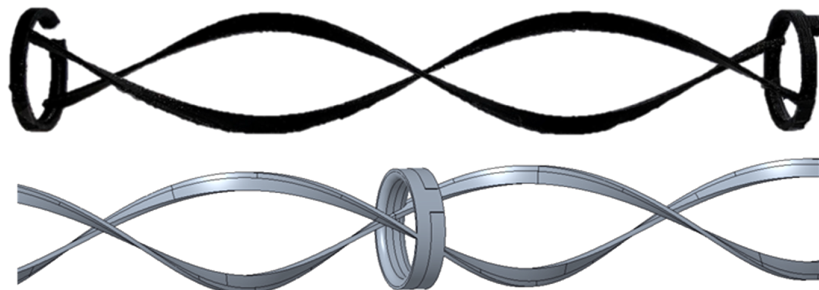


Figure 4. 3D-print of a helical fin module (top) and snapshot of the CAD model (bottom).

2.1.2. Particle Count and Pressure Drop Measurements

For the pressure drop measurements, a reactor tube with a diameter of $D = 24.14$ mm, which is slightly below the nominal diameter reported in Section 2, and height of $H = 600$ mm was filled manually with particles. The particle number N_p was calculated according to the weighing method described by Dixon [30], using Equation (1), where m_p is the total mass of particles in the reactor, ρ_p the particle density, which was estimated from weighing 100 particles, and the particle diameter d_p .

$$N_p = \frac{6m_p}{\rho_p \pi d_p^3} \quad (1)$$

The experimental setup for the pressure drop measurements is shown schematically in Figure 5. The mass flow controller (MFC) from Bronkhorst High-Tech B.V., AK Ruurlo, Netherlands (Model: F-202AV-M10-AGD-55-V) was operated in a range of normal volume flow rates (based on $T = 0$ °C and $p = 1$ atm) from 2 to 60 LN min⁻¹. The MFC accuracy is described with a value of $\pm 0.5\%$ of the actual value plus $\pm 0.1\%$ of full scale. Nitrogen was used as a working gas with a head pressure above the fixed bed from 950 to 1400 mbar. The pressure drop was measured using two pressure sensors from Swagelok Company, Solon, OH, USA (Model: PTI-S-AA2.5-11AQ) with an accuracy of 0.25 of span best fit straight line, located at the top and bottom of the fixed bed. Additionally, the temperature of the nitrogen was measured. Using the temperature, head pressure, and normal flow rate, the inlet velocity for the CFD simulation was calculated based on the ideal gas law. The pressure drop data reported hereafter are corrected with the pressure drop in the setup without the bed structure.

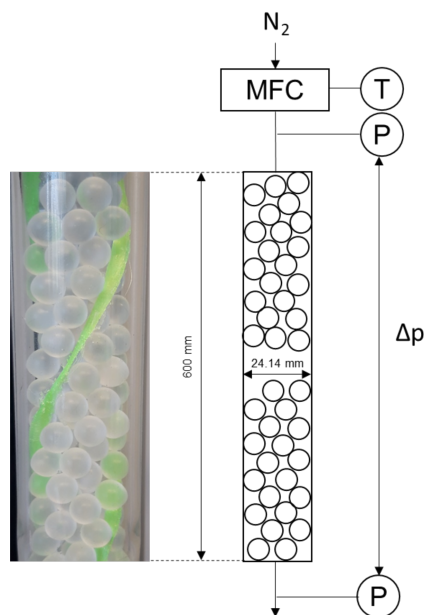


Figure 5. Experimental setup of the pressure drop measurements: details of the bed structure with 3D printed heat fins (**left**) and sketch of the experimental setup (**right**).

2.2. Numerical Methods

In recent years, particle-resolved CFD simulations of packed bed reactors have become a valuable and predictive tool to describe the fluid dynamics and transport processes in a fully spatially resolved manner. The review articles of Jurtz et al. [31] and Dixon et al. [32,33] provide a broad overview of this fast developing topic. The basic steps for this kind of CFD simulation are:

- The generation of a random particle packing
- The construction of a CAD description of the packing
- Meshing of the geometry
- The CFD simulation itself

The workflow developed by Eppinger et al. [34] is used in this study. It uses the Discrete Element Method (DEM) to numerically generate the particle bed. Based on the position of the spherical particles, a CAD description is generated and meshed using the local “caps” strategy. A more detailed description of the process can either be found in the original literature or in Jurtz et al. [31]. All numerical simulations are conducted with the commercial CFD tool *Simcenter STAR-CCM+* provided by *Siemens PLM Software*.

2.2.1. Numerical Packing Generation

DEM is a numerical method established by Cundall and Strack [35]. For each particle Newton’s law of motion is solved to compute their trajectories. To calculate the contact forces, particles are allowed to overlap slightly. Restitution and damping forces are calculated based on the existing overlap. The linear momentum equation for each particle is given by:

$$m_p \frac{dv_p}{dt} = F_s + F_b, \quad (2)$$

whereby m_p is the particle mass, v_p the particle velocity, t is time and F_s and F_b are the sum of surface and body forces that act on the particle. Only the gravitational force, drag force and the contact forces are

considered in the filling simulations. The overall contact force is calculated as the sum of particle-particle and particle-wall contact forces that act on a particle. The contact force can be split up in a tangential ($F_{n,i}$) and a normal ($F_{t,i}$) acting component:

$$F_c = \sum_{i=0}^{\text{contacts}} (F_{n,i} + F_{t,i}). \quad (3)$$

With the normal spring stiffness K_n , the overlap in normal direction d_n , the normal damping N_n and the normal velocity component of the relative sphere surface velocity at the contact point v_n , the normal force can be calculated as:

$$F_n = -K_n d_n - N_n v_n. \quad (4)$$

The tangential force is defined as:

$$F_t = \begin{cases} -K_t d_t - N_t v_t & \text{for } |-K_t d_t| < |K_n d_n C_{fs}| \\ \frac{|K_n d_n| C_{fs} d_t}{|d_t|} & \text{for } |-K_t d_t| \geq |K_n d_n C_{fs}|. \end{cases} \quad (5a)$$

$$(5b)$$

Here, K_t is the tangential spring stiffness, d_t the overlap in tangential direction, N_t the tangential damping, v_t the tangential velocity component of the relative sphere surface velocity at the contact point and C_{fs} the static friction coefficient. The non-linear Hertz-Mindlin contact model is used in this study:

$$K_n = \frac{4}{3} E_{eq} \sqrt{d_n R_{eq}} \quad (6)$$

$$K_t = 8 G_{eq} \sqrt{d_n R_{eq}} \quad (7)$$

$$N_n = N_{n,damp} \sqrt{5 K_n M_{eq}} \quad (8)$$

$$N_t = N_{t,damp} \sqrt{5 K_t M_{eq}}. \quad (9)$$

Here, $N_{n,damp}$ and $N_{t,damp}$ are the normal and tangential damping coefficients that are calculated from the normal and tangential restitution coefficient $C_{n,rest}$ and $C_{t,rest}$:

$$N_{n,damp} = \frac{-\ln(C_{n,rest})}{\sqrt{\pi^2 + \ln(C_{n,rest})^2}} \quad (10)$$

$$N_{t,damp} = \frac{-\ln(C_{t,rest})}{\sqrt{\pi^2 + \ln(C_{t,rest})^2}}. \quad (11)$$

M_{eq} , R_{eq} , E_{eq} and G_{eq} are the equivalent values of mass, radius, Young's modulus and shear modulus of particles A and B during the collision:

$$M_{eq} = \frac{1}{\frac{1}{M_A} + \frac{1}{M_B}} \quad (12)$$

$$R_{eq} = \frac{1}{\frac{1}{R_A} + \frac{1}{R_B}} \quad (13)$$

$$E_{eq} = \frac{1}{\frac{1-\nu_A^2}{E_A} + \frac{1-\nu_B^2}{E_B}} \quad (14)$$

$$G_{eq} = \frac{1}{\frac{2(2-\nu_A)(1+\nu_A)}{G_A} + \frac{2(2-\nu_B)(1+\nu_B)}{G_B}}, \quad (15)$$

whereby ν is the Poisson ratio.

The angular momentum of each particle is conserved as well by:

$$I_p \frac{d\omega_p}{dt} = \sum_{i=0}^{\text{contacts}} (r_c \times F_{c,i} + M_{c,i}). \quad (16)$$

here, I_p is the particle moment of inertia, ω_p the angular velocity, r_p the position vector from particles center of gravity to the contact point and M_c the acting moment due to rolling resistance:

$$M_c = -C_{fr} |r_c| |F_c| \frac{\omega_p}{|\omega_p|}. \quad (17)$$

C_{fr} is the rolling friction coefficient.

In our study, the drag force is considered to prevent particles to accelerate to nonphysically high velocities. The Schiller-Naumann drag correlation [36] is used, whereby, the particle velocity corresponds to the relative velocity as the flow field is not solved for the filling simulations.

For a better comparability between experimental and numerical results, we restrict our investigations to dense packed beds. To numerically mimic the process of bed densification that is done in the experiment, we manipulate the static friction coefficient, as recently suggested by Jurtz et al. [26]. All simulation parameter for the DEM simulations are given in Table 2.

Table 2. DEM parameters used.

Property	Value
Young's modulus [MPa]	100.0
Poisson ratio [-]	0.45
Static friction coefficient [-]	0.01
Rolling friction coefficient [-]	0.001
Restitution coefficients [-]	0.5
Particle density [kg/m ³]	1100.0

2.2.2. Computational Fluid Dynamics

For the CFD simulations, the steady-state mass, momentum and energy conservation equations are solved using the Finite Volume Method:

$$\nabla \cdot (\rho v) = 0 \quad (18)$$

$$\nabla \cdot (\rho v v) = \nabla T \quad (19)$$

Here ρ is mass density of the fluid, v fluid velocity and T the stress tensor:

$$T = - \left(p + \frac{2}{3} \mu \nabla \cdot v \right) I + 2\mu D, \quad (20)$$

where p is pressure, μ dynamic viscosity, I the unit tensor and D the deformation tensor, given as:

$$D = \frac{1}{2} \left[\nabla v + (\nabla v)^T \right]. \quad (21)$$

The energy equation is solved using the specific enthalpy h :

$$\nabla \cdot (\rho h v) = -\nabla \cdot \dot{q} + (\tau : \nabla v) - p (\nabla \cdot v) \quad (22)$$

whereas the convective term and the work terms are neglected in the solid phase, and only the conductive term $\dot{q} = -\lambda \nabla T$ is solved. The Realizable $k-\varepsilon$ turbulence model with an all y^+ wall treatment is used to consider turbulent effects. This model has already been successfully used in our previous studies [10,34,37,38]. The ideal gas equation of state is used to account for compressible effects. At the fluid-solid interface the conjugated heat transfer is solved by ensuring invariance of heat fluxes.

Polyhedral cells are used to discretize the domain, whereas a conformal mesh interface is generated between the gas and solid phases. During the meshing process, locally, small gaps are introduced between touching particles and between particles and the wall, as proposed by Eppinger et al. [34]. In comparison to other contact modification methods (e.g., bridging particle contacts) this method can be applied for heat transfer simulations without having to specify an additional thermal resistance at the contact points [39]. To minimize the influence of the inlet and outlet boundary conditions, the volume mesh is extended by extruding the inlet and outlet. Recently, Minhua et al. [40] published a mesh refinement study, showing that the mesh settings used lead to an almost mesh-independent solution, even for locally evaluated properties. This has also been shown by our research group, earlier [38,41]. The total cell count is up to 11.5 million for the fluid dynamic simulations, where the inner of the particles are not meshed, and up to 22.3 million if the heat transfer is considered and the solid parts are resolved with a grid.

3. Results and Discussion

3.1. Experimental Validation

A comparison between the experimentally and numerically determined number of particles within a bed height of $H = 600$ mm is given in Table 3. For the reactor without internals, the average particle count is 827, having a maximum deviation of $\pm 0.12\%$. An excellent agreement with the synthetically generated bed is observed that has a particle count of 823. A slightly higher spreading of particle count is observed for the reactor with helical fins. The average number of particles is 746 with a maximum deviation of $\pm 0.6\%$. Nevertheless, this can be considered as a good reproducibility, and the particle count of the numerically generated bed, which is 745, is very close to the mean number. Main reason for the increasing deviation in particle count for the reactor with fins are the support rings, as below the rings additional voids can arise, if the filling is carried out too fast.

Table 3. Comparison of the particle count ($H = 600$ mm) between experimental and DEM results.

	Particle Count				DEM
	Exp. #1	Exp. #2	Exp. #3	Exp. #4	
Without fins	826	826	828	827	823
Helical fins	750	747	741	-	745

The simulated and experimentally determined specific pressure drop is compared in Figure 6. For a wide range of particle Reynolds numbers an excellent agreement can be observed. A maximum deviation of 15% was observed for the case without internals at the lowest inlet velocity. For the remaining simulations the relative deviation is below 10%, with an average relative deviation of 6.7% for the reactor without fins and 4.5% for the helical fin design, respectively.

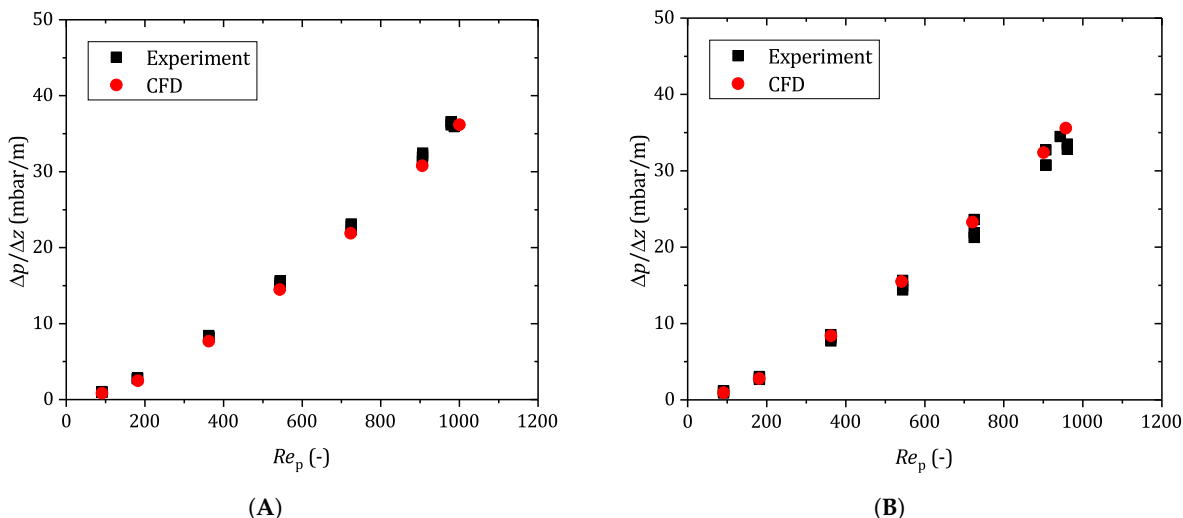


Figure 6. Predicted specific pressure drop in comparison to experimental results for (A) the reactor without heat fins, and (B) the reactor with helical fins.

For a better comparability of the two investigated designs, the numerical results are fitted towards a Darcy-Forchheimer type equation, resulting in the following description:

$$\left(\frac{\Delta p}{\Delta z}\right)_{\text{No Fin}} = 0.28466 \cdot u_0 + 13.94474 \cdot u_0^2 \tag{23}$$

$$\left(\frac{\Delta p}{\Delta z}\right)_{\text{Helical Fin}} = 0.73153 \cdot u_0 + 14.18691 \cdot u_0^2. \tag{24}$$

Based on Equations (23) and (24), Figure 7 compares the specific pressure drop of the two designs. The use of helical heat fins lead to an increasing pressure drop. However, for the investigated range of Reynolds numbers ($100 < Re_p < 1000$) the increase is below 10%, whereby, with increasing Reynolds number, differences vanish. For conditions that are most probably out of scope of industrial applications ($Re_p < 100$) the helical fin leads to a significantly higher pressure drop, which can be attributed to the higher value of the viscous term in Equation (24). A possible reason for this, which will be discussed in more detail in the following section, is the formation of a strong swirl near the reactor wall, which is caused by the helical fins. This causes an increase of average tortuosity leading to higher viscous frictional losses. Contrarily, the influence of the helical fins on the pressure drop decrease with increasing Re_p . This is due to the fact that the main driver is then the deflection of flow through the bed structure.

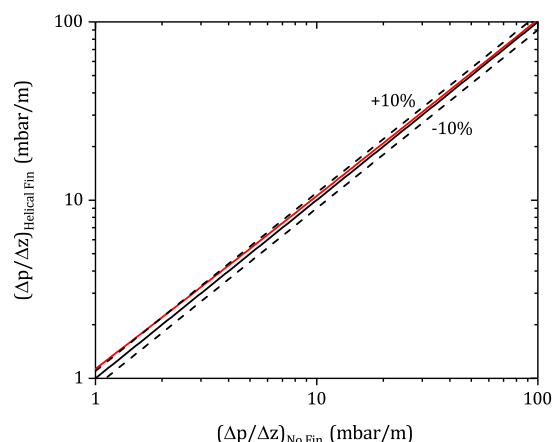


Figure 7. Parity plot, comparing the specific pressure drop of the reactor without fins, and the one with helical fins. The provided data is based on polynomial fitting of the simulation data according to Equations (23) and (24).

3.2. Detailed Numerical Study

In the experimental study multiple modules were used, as for the reason of stability, the two fins need to be fixed using two annular connection elements. The connection elements are neglected in the further part of this study in order to reduce the level of complexity. Furthermore, it is assumed that the fins are made of stainless steel, a material characterized by its good thermal conductivity, and that can be used for conventional and additive manufacturing processes. A packed bed without heat fins is compared against reactors with straight and with helical heat fins regarding the bed morphology, the fluid dynamics and the heat transfer characteristic. The dimensions of the fins and the container correspond to the nominal values given in Section 2. The boundary conditions are summarized in Table 1.

3.2.1. Bed Morphology

As the fluid dynamics, and likewise, the heat transfer is strongly coupled with the bed morphology, first, the impact of the heat fins on the particle arrangement is investigated. A bed voidage of $\varepsilon = 0.460$ is observed for the design without additional heat fins. The usage of heat fins significantly increases the bed voidage to values of $\varepsilon = 0.470$ for the straight fin design and $\varepsilon = 0.491$ for the helical design, respectively. In other words, the specific surface area without fins is 465 m^{-1} , whereas it is 431 m^{-1} for a bed with helical fins and 444 m^{-1} for a bed with straight fins. This is obvious, because additional particle-wall contacts are created. The radial void fraction distributions, given in Figure 8, show that this effect is limited to the near wall region, which extend until one particle diameter away from the wall. Here, the straight and helical fin designs show a similar increased void fraction in comparison to the reactor without heat fins. At a position of $r^* = (R - r) / d_p \approx 0.6$, a discontinuity is observed, leading to a small, but recognizable, increase of void fraction. This corresponds to the position of the fin tips. For the straight fin design, Figure 9 shows, based on a parallel projected view from the top of the reactor, a transmitted light image of all particles that are in contact with the wall. The one sphere near the center of the bed is in contact with the bottom plate of the reactor. It can be seen that the majority of particles are arranged between the two heat fins and only a small number is in contact with the tip of the fins itself. This results in the observed steep increase of void fraction close to the fin tips. However, after a distance of one until one and a half particle diameters, the straight fin design shows the lowest void fraction, while the helical design and the reactor without fins show similar values. In the core of the bed, the reactor without fins has the lowest void fraction, while the straight design shows the highest values. The coincident trends of the radial void fraction profiles near the

wall show that there is no increase in particle-wall contacts for the helical design compared to the straight design, although this could have been expected. Furthermore, it can be seen that away from the wall, the impact of fins on bed voidage is low.

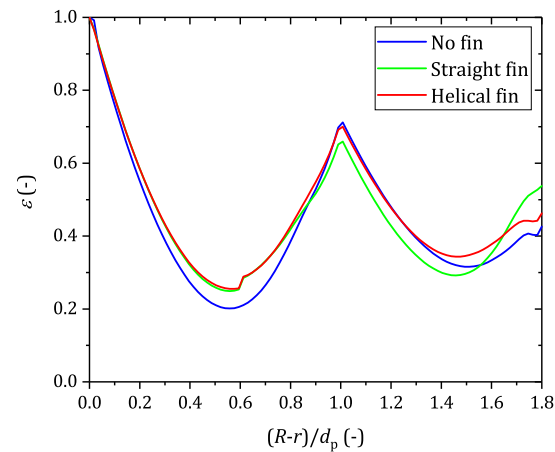


Figure 8. Radial void fraction distribution for the different investigated designs.

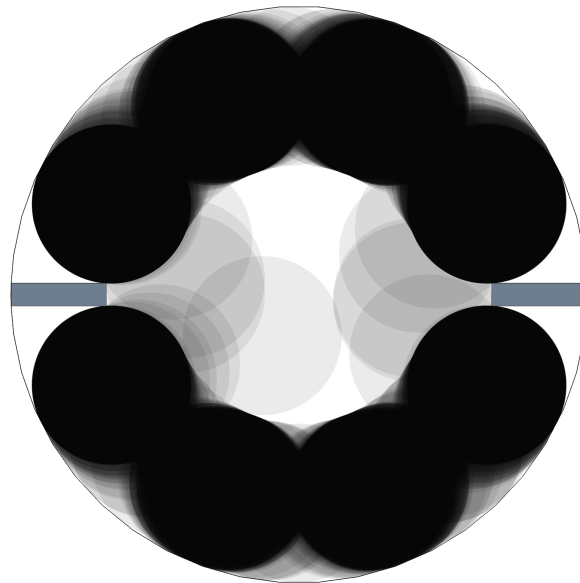


Figure 9. Transmitted light image of particles that have wall contacts (straight fin design).

3.2.2. Fluid Dynamics

The observed differences in bed morphology significantly impact the fluid dynamics of the different reactor designs. Figure 10 shows the radial profiles of the axial and tangential absolute velocity, normalized with the local interstitial velocity for different particle Reynolds numbers. For all investigated designs, the wall channeling effect is clearly visible, leading to a peak in axial velocity at a dimensionless wall distance of $r^* \approx 0.1$. In comparison to the other designs, the straight fin design shows a significant higher axial velocity close to the wall. This is caused by the additional interstices between particles, fin and reactor wall that can be seen in Figure 9. This leads to an additional extreme channeling effect as the flow can pass straight through the reactor. The helical design is characterized by a distinct swirl close

to the wall, as can be seen in the profile of the tangential velocity. With increasing Reynolds number the swirl gets more distinct. However, this effect is limited to $r^* \leq 0.6$, which corresponds to the fin width. However, the flow in this near wall region is in strong exchange with flow in the center of the bed as can be seen in Figure 11. Here, intersection points of streamlines with cross-sectional planes at a distance of 10 mm are shown, whereas the streamlines were injected in the annular space near the wall at a bed height of 100 mm. It can be seen that due to the presence of particles, the flow gets quickly dispersed, which is important for the convective radial heat transfer. At high Reynolds numbers, Figure 10 shows for the reactor without internals close to the wall a slight increase of tangential velocity as well, while for the straight-fin design this effect can not be observed. This is mainly caused by the straight channeling effect discussed before.

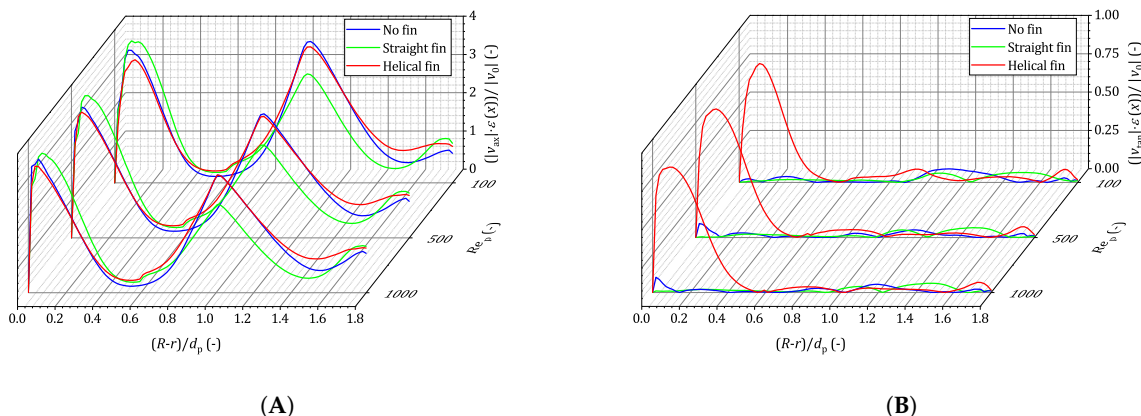


Figure 10. Radial profiles of the circumferentially and axially averaged absolute value of (A) axial and (B) tangential velocity, which are normed to the local interstitial velocity.

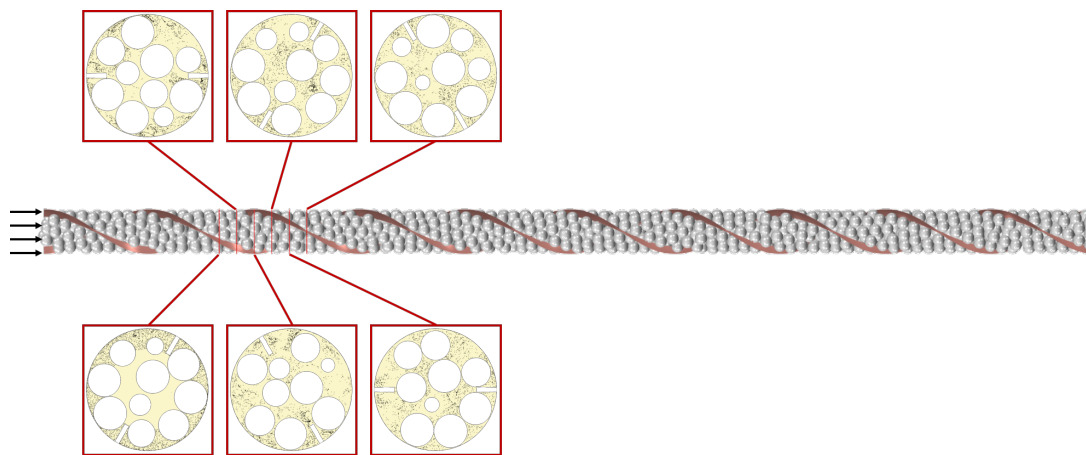


Figure 11. Helical design: Visualization of the intersection points of streamlines with cross-sectional planes at a distance of 10 mm. The streamlines were injected in the annular space near the wall at a bed height of 100 mm.

The second maximum of the axial velocity coincides with the maximum of the radial void fraction distribution, that is given in Figure 8, at a position of $r^* \approx 1.0$. Due to the extreme wall channeling that was found for the straight design, for continuity reasons, a reduced axial velocity is observed in comparison to the other two designs. In the center of the bed a further increase of axial velocity can be found for the straight-fin design, which results from the pronounced increase of void fraction that was found. For the

reactor without internals and the helical-fin design only a slight increase in axial velocity can be observed in the core of the bed.

The specific pressure drop for the different designs is listed in Table 4. Caused by the higher bed voidage and increased wall and core channeling, the pressure drop of the straight-fin design is significantly lower, compared to the baseline design without internals. A reduction between 20–30% is found. Considering Ergun’s equation [42], as the bed voidage is about 2% higher compared to the baseline design, around 10% of the pressure drop reduction can be attributed to the increase in bed voidage, while the remaining amount must be addressed to the additional channeling effects. The additional channeling effects are reflected by a lower friction factor Ψ , as can be seen in Table 4. The helical design shows a specific pressure drop similar to the one of the reactor without internals. However, as the bed voidage is about 7% higher for the helical-fin design, a significant pressure drop reduction would normally be expected. In fact, it is found that the friction factor increases by 30%. The, in relation to the bed voidage, increased pressure drop can be attributed to the strong swirl that was found close to the wall. This leads to a more tortuous flow path.

Table 4. Summary of simulation results.

Re_p	Design	$\Delta p/\Delta z$ (Pa/m)	$\delta_{\Delta p}$ (%)	$\Psi = \frac{\Delta p}{\rho_f u_0^2} \cdot \frac{d_p}{L} \cdot \frac{\varepsilon^3}{1-\varepsilon}$ (-)	δ_Ψ (%)	α_w (W/(m ² K))	δ_{α_w} (%)	$\lambda_{r,eff}$ (W/(m K))	$\delta_{\lambda_{r,eff}}$ (%)
1056	No fin	192.0	-	4.17	-	29.5	-	0.149	-
	Straight fin	157.9	-18	4.01	-4	32.0	+8	0.189	+27
	Helical fin	193.9	+1	5.43	+30	37.5	+25	0.219	+47
528	No fin	2755.4	-	2.41	-	73.3	-	0.461	-
	Straight fin	1950.8	-29	1.98	-18	86.9	+19	0.449	-3
	Helical fin	2804.6	+2	3.14	+30	98.7	+35	0.769	+67
1056	No fin	9721.9	-	2.11	-	124.3	-	0.831	-
	Straight fin	6600.2	-32	1.68	-20	140.5	+13	1.082	+30
	Helical fin	10,072.8	+4	2.82	+34	149.9	+21	1.573	+89

3.2.3. Heat Transfer

The axial profiles of the dimensionless temperature $\Theta = (T - T_0) / (T_w - T_0)$ in the center of the bed, as well as the axial profile of the mass flow averaged temperature, evaluated on cross sectional planes, are given in Figure 12. For the lowest Reynolds number it can be seen that, until an axial distance of approximately $10 d_p$, the core temperature profiles of the straight-fin design and the baseline design are almost coincident. After that position, the temperature gradients for the straight-fin design get steeper in comparison to the baseline case, leading to higher core temperature at same axial positions. With increasing Reynolds number the position increases slightly to a value of $20 d_p$, nevertheless, the trend of higher core temperatures is still preserved, indicating an improved heat transport characteristic. The axial profile of the mass flow averaged temperature show that, except for the position $10 \leq z/d_p \leq 15$, always higher average temperatures are found for the straight-fin design. For the helical-fin design this trend is even more pronounced. Besides a small entry length of $\leq 5 d_p$, the core and the average temperatures are significantly above those of the other investigated designs, which is a first indicator for the superior heat transfer characteristic of the helical-fin design.

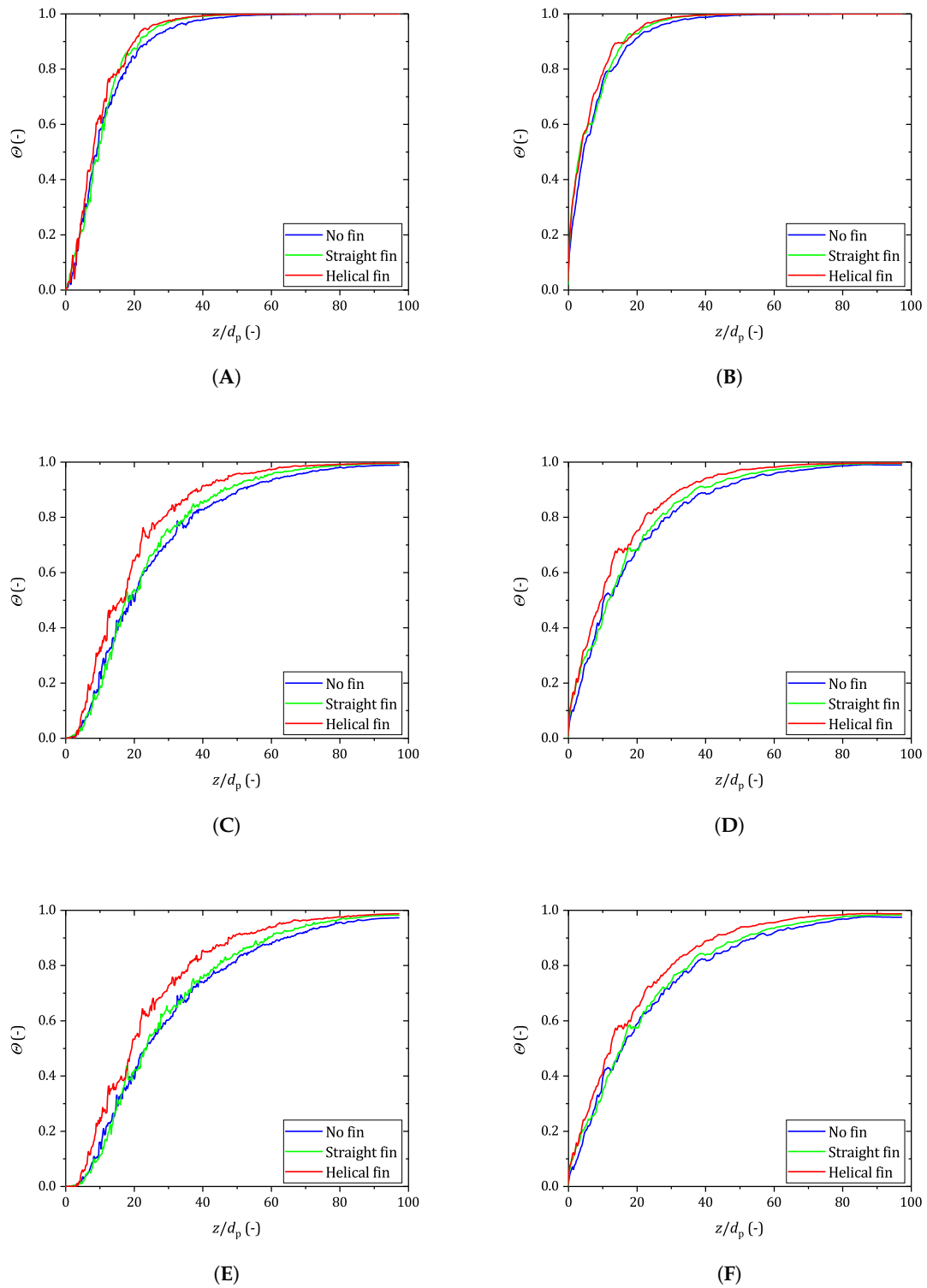


Figure 12. Comparison of the axial profile of the core temperature (left) and the averaged temperature (right) for $Re_p = 105.6$ (A,B), $Re_p = 528$ (C,D) and $Re_p = 1056$ (E,F).

Based on the axial profile of the logarithmized dimensionless core temperature $\Theta_{\log,c} = \ln [(T_w - T_c) / (T_w - T_0)]$, the wall heat transfer coefficient and the effective radial thermal conductivity can be calculated from the slope and the intercept of the resulting straight line as described by Wakao and Kaguei [43]:

$$\text{slope} = -a_1^2 \left(\frac{\lambda_{r,\text{eff}}}{v_0 \rho_f c_{p,f} R^2} \right) \quad (25)$$

$$\text{intercept} = \ln \frac{2}{a_1 \left[1 + (a_1 / Bi)^2 \right] J_1(a_1)} \quad (26)$$

First, the parameter a_1 is determined iteratively, solving:

$$\frac{T_w - T_m}{T_w - T_c} = \frac{2J_1(a_1)}{a_1} \quad (27)$$

at the end of the bed. Once a_1 is known, the effective radial thermal conductivity and Biot number $Bi = \alpha_w R / \lambda_{r,\text{eff}}$ can be calculated from Equations (25) and (26). In a last step, the wall heat transfer coefficient is calculated from the Biot number. In above's equations, ρ_f and $c_{p,f}$ are the density and specific heat of the gas phase, T_c the core temperature, T_m the average exit temperature, and $J_1(a_1)$ the Bessel function of first kind and first order. The underlying assumptions of this evaluation method is, that axial heat conduction can be neglected, which is true for high flow rates. For a more detailed description the interested reader is referred to the original literature [43]. For the fitting of the linear temperature curve only temperature values of $0.05 \leq \Theta \leq 0.95$ are considered, to minimize thermal entry and saturation effects. Based on the simulation of the baseline design at $u_0 = 1.1$ m/s the sensitivity of α_w and $\lambda_{r,\text{eff}}$ towards the accounted temperature range was conducted, whereas the range of Θ was varied as follows: $\{\Theta \in \mathbb{R} : 0.02 \leq \Theta \leq 0.4 \wedge 0.6 \leq \Theta \leq 0.98\}$. The mean relative deviation for α_w and $\lambda_{r,\text{eff}}$ were 1% and 6%, respectively. To ensure a representative number of data points to be evaluated, we decided to use the reported range of Θ .

The calculated wall Nusselt numbers and dimensionless effective radial thermal conductivities are given in Figure 13 and are compared with the correlation values of Yagi and Kunii [2,44]. For the baseline design, the values for α_w and $\lambda_{r,\text{eff}}$ tend to be a bit lower in comparison to the correlations. However, considering the scattering of literature values that were reported by Dixon [45], the agreement is satisfactory. Furthermore, the results show the positive effect of the internal heat fins on both, the wall Nusselt number and the effective radial thermal conductivity. As summarized in Table 4 α_w increases by 8–19% and 21–35% for the straight and helical fin design, respectively. The increase in $\lambda_{r,\text{eff}}$ is approximately 47–89% for the helical design, whereas the gain gets larger for higher Reynolds numbers. Not so clear are the results for the straight fin design. While a growth in $\lambda_{r,\text{eff}}$ of around 30% can be seen for $Re_p \approx 100$ and $Re_p \approx 1000$, no performance gain was found for $Re_p \approx 500$. The reason for this could yet not be identified, nevertheless, the results show the beneficial impact of internal heat fins on the overall heat transfer. Since the heat fins change both, the flow field and the bed morphology (see: Figures 8 and 10), it is hard to distinguish which heat transfer mechanism exactly improves the thermal performance. However, the results of the straight fin design show slight additional channeling effects close to the wall that are induced by the higher voidage in that area. Theoretically, this would negatively affect the radial heat transport in this area. The fact, that the thermal performance is also increased for that fin design indicates, that the gain of radial heat transfer can significantly be attributed to the conduction through the solid of the fins.

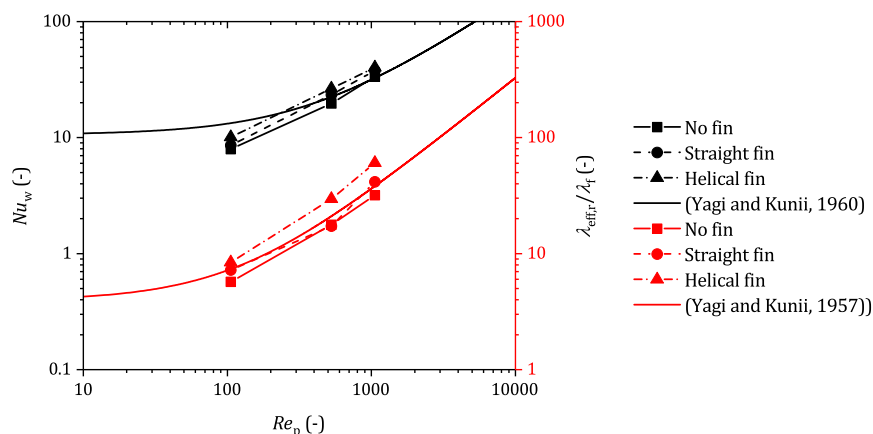


Figure 13. Wall Nusselt number (black) and the dimensionless effective radial thermal conductivity (red) as a function of particle Reynolds number for all investigated designs in comparison to the correlations of Yagi and Kunii [2,44].

4. Conclusions

In this work, the impact of internal heat fins on the bed morphology, pressure drop and heat transfer in slender packed bed reactors filled with spherical particles was investigated. Helical fin modules were manufactured using the FLM 3D printing technique. The effect of the fins on bed morphology, in terms of particle count, and specific pressure drop was investigated both, experimentally and numerically, using particle-resolved CFD. An excellent agreement between the CFD results and the experimental measurements were found, indicating that particle-resolved CFD is a reliable and predictive tool that can be used for further design studies, e.g., dimensions, shape, and numbers of internal heat fins. For industrially relevant Reynolds numbers ($Re_p > 100$), the specific pressure drop, caused by the helical heat fins, is below +10% in comparison to the case without fins. However, one needs to keep in mind, that the bed voidage increases due to the presence of the helical fins, resulting in a lower pellet surface area per reactor volume.

In a comparative numerical study, two different heat fin designs (helical and straight fin design) were compared against a reactor without heat fins under wall-heated conditions. While, in accordance with our previously presented results, the specific pressure drop for the helical fin design is only slightly increased, a significant reduction in specific pressure drop of 20% was observed for the straight fin design. To account for the differences in bed voidage, the friction factors were calculated. A decrease of up to 20% can be seen for the straight fin design, which is mainly caused by additional channeling effects that are a result of how the spherical particles arrange around the heat fins. Regarding the helical fin design, a strong swirl occurs close to the tube wall, which is the main driving force for the increase of the friction factor of 30%. Nevertheless, it was found that the flow in this near-wall region is in strong exchange with the flow in the remaining bulk part of the reactor.

Based on the axial temperature profiles, the wall heat transfer coefficients and the effective radial thermal conductivities were calculated. Over the investigated particle Reynolds number range, an increase of 25% to 35% in wall heat transfer coefficient, and of up to almost 90% in effective radial thermal conductivity was found for the helical fin design, respectively. For the straight fin design, the increase of the wall heat transfer coefficient accounts for 8–19%. For the lowest and highest investigated Reynolds number, also for the straight fin design, a significant increase in $\lambda_{r,eff}$ of up to 30% was found. Overall, the simulation results show the beneficial impact of internal heat fins on the heat transfer characteristics in slender packed bed reactors. In comparison to other presented reactor concepts, the advantages of internal heat fins are:

- It is applicable to new and already existing reactors, as the fins are manufactured as replaceable sleeves.
- The morphological and fluid dynamic characteristics (bed voidage and pressure drop) change only moderately.
- The active catalytic surface area changes only slightly. It is reduced by 7% for the helical and below 5% for the straight fin design, respectively.
- Reactor filling and re-filling strategies can stay unaffected.

Nevertheless, we see the following future tasks, to make this a reliable reactor concept:

- Although, some publications are available, indicating the accuracy of particle-resolved CFD when it comes to heat transfer simulation, e.g., [46,47], broader validation is necessary, to make this a reliable and predictive design tool, especially under industrial conditions, e.g., complex particle shapes, turbulent flows, steep gradients, and coupled with catalytic reactions.
- Design parameters, such as number of fins, fin thickness, fin material and fin shape, should be varied to find an optimized fin design that incorporates a beneficial heat transfer characteristic with a reduced impact on bed voidage, active catalytic surface area and pressure drop.
- It needs to be evaluated, if a generalized optimized fin design can be found, that is also applicable to other particle shapes than spheres, or if individual solutions must be developed.
- Possible limits regarding the manufacturability using 3D printing need to also be evaluated.

Author Contributions: Conceptualization, N.J., M.K. and G.D.W.; methodology, N.J. and G.D.W.; validation, N.J., S.C.S. and S.F.; formal analysis, N.J. and S.F.; investigation, N.J., S.C.S. and S.F.; writing—original draft preparation, N.J., S.C.S., S.F., M.K. and G.D.W.; writing—review and editing, N.J., S.C.S., S.F., M.K. and G.D.W.; visualization, N.J., S.C.S., S.F. and G.D.W.; supervision, M.K. and G.D.W. All authors have read and agreed to the published version of the manuscript.

Funding: This research received no external funding.

Conflicts of Interest: The authors declare no conflict of interest.

Abbreviations

The following abbreviations are used in this manuscript:

CAD	Computer aided design
CFD	Computational fluid dynamics
DEM	Discrete element method
FLM	Fused layer modeling
MFC	Mass flow controller
PLA	Polyactid
POCS	Periodic open-cell structures
PVA	Polyvinylalcohol

Nomenclature

C_{fr}	rolling friction coefficient	[-]
C_{fs}	static friction coefficient	[-]
$C_{n,rest}$	normal restitution coefficient	[-]
$C_{t,rest}$	tangential restitution coefficient	[-]
D	tube diameter	[m]
E_{eq}	particle equivalent Young's modulus	[Pa]
G_{eq}	particle equivalent shear modulus	[Pa]

H	bed height	[m]
$J_1()$	Bessel function of first kind and first order	[-]
K_n	normal spring stiffness	[N m ⁻¹]
K_t	tangential spring stiffness	[N m ⁻¹]
M_{eq}	particle equivalent mass	[kg]
N	tube-to-particle diameter ratio	[-]
$N_{n,damp}$	normal damping coefficient	[-]
N_n	normal damping	[N s m ⁻¹]
N_p	particle count	[-]
$N_{t,damp}$	tangential damping coefficient	[-]
N_t	tangential damping	[N s m ⁻¹]
R	tube radius	[m]
R_{eq}	particle equivalent radius	[m]
T	temperature	[K]
T_0	inlet temperature	[K]
T_c	core temperature	[K]
T_m	average outlet temperature	[K]
T_w	wall temperature	[K]
V_{POCS}	volume of the POCS	[m ³]
$V_{p,total}$	volume of all particles	[m ³]
V_{total}	empty reactor volume	[m ³]
\mathbf{D}	deformation tensor	[s ⁻¹]
\mathbf{F}_b	body forces	[N]
\mathbf{F}_n	normal contact force	[N]
\mathbf{F}_s	surface forces	[N]
\mathbf{F}_t	tangential contact forces	[N]
I_p	particle moment of inertia	[kg m ⁻²]
\mathbf{I}	unit tensor	[-]
\mathbf{M}_c	moment due to contact	[N m]
\mathbf{T}	stress tensor	[Pa]
\mathbf{r}_p	position vector from particle center of gravity to contact point	[m]
\mathbf{v}_p	particle velocity	[m s ⁻¹]
\mathbf{v}	fluid velocity	[m s ⁻¹]
\mathbf{q}	conductive heat flux	[W m ⁻²]
a_1	parameter	[-]
a_v	specific surface area	[m ⁻¹]
$c_{p,f}$	fluid specific heat	[J kg ⁻¹ K ⁻¹]
d_n	overlap in normal direction	[m]
d_{pore}	pore diameter	[m]
d_p	particle diameter	[m]
d_t	overlap in tangential direction	[m]
h	specific enthalpy	[J kg ⁻¹]
i	contact index	[-]
m_p	particle mass	[m ³]
p	pressure	[Pa]
r	radial coordinate	[m]

r^*	dimensionless wall distance	[-]
t	time	[s]
v_0	superficial velocity	[m s ⁻¹]
v_n	normal velocity component of the relative sphere surface velocity	[m s ⁻¹]
v_t	tangential velocity component of the relative sphere surface velocity	[m s ⁻¹]
z	axial coordinate	[m]
Ψ	friction factor	[-]
Θ	dimensionless temperature	[-]
$\Theta_{\log,c}$	dimensionless logarithmic core temperature	[-]
α_w	wall heat transfer coefficient	[W m ⁻² K ⁻¹]
ω_p	particle angular velocity	[rad s ⁻¹]
δ	relativ deviation	[%]
λ	thermal conductivity	[W m ⁻¹ K ⁻¹]
$\lambda_{r,eff}$	effective radial thermal conductivity	[W m ⁻¹ K ⁻¹]
μ	dynamic viscosity	[Pa s]
ν	Poisson ratio	[-]
ρ	fluid density	[kg m ⁻³]
ρ_f	fluid density	[kg m ⁻³]
ρ_p	particles solid density	[kg m ⁻³]
ε	void fraction	[-]
ε_{foam}	foam voidage	[-]

Dimensionless Numbers

$Bi = \alpha_w R / \lambda_{r,eff}$	Biot number
$Re_p = v_0 d_p \rho_f / \mu_f$	particle Reynolds number
$Nu_w = \alpha_w d_p / \lambda_f$	wall Nusselt number

References

1. Eigenberger, G. Principles of chemical reaction engineering and plant design. In *Ullmann's Encyclopedia of Industrial Chemistry, Principles of Chemical Reaction Engineering and Plant Design*, 5th ed.; Elvers, B., Ed.; Wiley VCH: Weinheim, Germany, 1992; Chapter B4, pp. 199–238. [\[CrossRef\]](#)
2. Yagi, S.; Kunii, D. Studies on heat transfer near wall surface in packed beds. *AIChE J.* **1960**, *6*, 97–104. [\[CrossRef\]](#)
3. Giese, M.; Rottschäfer, K.; Vortmeyer, D. Measured and modeled superficial flow profiles in packed beds with liquid flow. *AIChE J.* **1998**, *44*, 484–490. [\[CrossRef\]](#)
4. Caulkin, R.; Jia, X.; Fairweather, M.; Williams, R.A. Predictions of porosity and fluid distribution through nonspherical-packed columns. *AIChE J.* **2012**, *58*, 1503–1512. [\[CrossRef\]](#)
5. Wehinger, G.D.; Eppinger, T.; Kraume, M. Evaluating catalytic fixed-bed reactors for dry reforming of methane with detailed CFD. *Chem. Ing. Tech.* **2015**, *87*, 734–745. [\[CrossRef\]](#)
6. Martin, H.; Nilles, M. Radiale Wärmeleitung in durchströmten Schüttungsrohren. *Chem. Ing. Tech.* **1993**, *65*, 1468–1477. [\[CrossRef\]](#)
7. Karthik, G.; Buwa, V.V. A computational approach for the selection of optimal catalyst shape for solid-catalysed gas-phase reactions. *React. Chem. Eng.* **2020**, *5*, 163–182.
8. Partopour, B.; Dixon, A.G. Effect of particle shape on methanol partial oxidation in a fixed bed using CFD reactor modeling. *AIChE J.* **2020**, *66*, e16904. [\[CrossRef\]](#)
9. Afandizadeh, S.; Foumeny, E. Design of packed bed reactors: Guides to catalyst shape, size, and loading selection. *Appl. Therm. Eng.* **2001**, *21*, 669–682. [\[CrossRef\]](#)

10. Jurtz, N.; Wehinger, G.D.; Srivastava, U.; Henkel, T.; Kraume, M. Validation of pressure drop prediction and bed generation of fixed-beds with complex particle shapes using discrete element method and computational fluid dynamics. *AIChE J.* **2020**, *66*, e16967. [[CrossRef](#)]
11. Lämmermann, M.; Horak, G.; Schwieger, W.; Freund, H. Periodic open cellular structures (POCS) for intensification of multiphase reactors: Liquid holdup and two-phase pressure drop. *Chem. Eng. Process. Process Intensif.* **2018**, *126*, 178–189. [[CrossRef](#)]
12. Lämmermann, M.; Schwieger, W.; Freund, H. Experimental investigation of gas-liquid distribution in periodic open cellular structures as potential catalyst supports. *Catal. Today* **2016**, *273*, 161–171. [[CrossRef](#)]
13. Busse, C.; Freund, H.; Schwieger, W. Intensification of heat transfer in catalytic reactors by additively manufactured periodic open cellular structures (POCS). *Chem. Eng. Process.-Process Intensif.* **2018**, *124*, 199–214. [[CrossRef](#)]
14. Ambrosetti, M.; Bracconi, M.; Maestri, M.; Groppi, G.; Tronconi, E. Packed foams for the intensification of catalytic processes: Assessment of packing efficiency and pressure drop using a combined experimental and numerical approach. *Chem. Eng. J.* **2020**, *382*, 122801. [[CrossRef](#)]
15. Fratallocchi, L.; Groppi, G.; Visconti, C.G.; Lietti, L.; Tronconi, E. Adoption of 3D printed highly conductive periodic open cellular structures as an effective solution to enhance the heat transfer performances of compact Fischer-Tropsch fixed-bed reactors. *Chem. Eng. J.* **2020**, *386*, 123988. [[CrossRef](#)]
16. Ambrosetti, M.; Groppi, G.; Schwieger, W.; Tronconi, E.; Freund, H. Packed Periodic Open Cellular Structures—An Option for the Intensification of Non-Adiabatic Catalytic Processes. *Chem. Eng.-Process.-Process. Intensif.* **2020**, *155*, 108057. [[CrossRef](#)]
17. Zobel, N.; Eppinger, T.; Behrendt, F.; Kraume, M. Influence of the wall structure on the void fraction distribution in packed beds. *Chem. Eng. Sci.* **2012**, *71*, 212–219. [[CrossRef](#)]
18. Eppinger, T.; Jurtz, N.; Kraume, M.; Zobel, N.; Frank, B. Influence of the Wall Structure On the Heat Transfer in Packed Beds with Small Tube to Particle Diameter Ratio. In Proceedings of the AIChE Annual Meeting, David L. Lawrence Convention Center, Conference Proceedings, Non-Topical Conferences, Pittsburgh, PA, USA, 28 October–2 November 2012; American Institute of Chemical Engineers: New York, NY, USA, 2012; p. 9.
19. Metzger, D.; Fan, C.; Haley, S. Effects of pin shape and array orientation on heat transfer and pressure loss in pin fin arrays. *J. Eng. Gas Turbines Power* **1984**, *106*, 252–257. [[CrossRef](#)]
20. Chyu, M.; Hsing, Y.; Shih, T.P.; Natarajan, V. Heat transfer contributions of pins and endwall in pin-fin arrays: Effects of thermal boundary condition modeling. *J. Turbomach.* **1999**, *121*, 257–263. [[CrossRef](#)]
21. Peles, Y.; Koşar, A.; Mishra, C.; Kuo, C.J.; Schneider, B. Forced convective heat transfer across a pin fin micro heat sink. *Int. J. Heat Mass Transf.* **2005**, *48*, 3615–3627. [[CrossRef](#)]
22. Nakaso, K.; Aoki, T.; Fukai, J. Effects of fin configuration on heat transfer rate in packed bed reactors for improvement of their thermal characteristics. In Proceedings of the International Heat Transfer Conference, Washington, DC, USA, 8–13 August 2010; Volume 49415, pp. 975–981.
23. Jeng, T.M.; Tzeng, S.C.; Huang, Q.Y. Heat transfer performance of the pin—fin heat sink filled with packed brass beads under a vertical oncoming flow. *Int. J. Heat Mass Transf.* **2015**, *86*, 531–541. [[CrossRef](#)]
24. Zhang, L.Z.; Wang, L. Effects of coupled heat and mass transfers in adsorbent on the performance of a waste heat adsorption cooling unit. *Appl. Therm. Eng.* **1999**, *19*, 195–215. [[CrossRef](#)]
25. Niazmand, H.; Dabzadeh, I. Numerical simulation of heat and mass transfer in adsorbent beds with annular fins. *Int. J. Refrig.* **2012**, *35*, 581–593. [[CrossRef](#)]
26. Jurtz, N.; Waldherr, P.; Kraume, M. Numerical Analysis of the Impact of Particle Friction on Bed Voidage in Fixed-Beds. *Chem. Ing. Tech.* **2019**, *91*, 1260–1266. [[CrossRef](#)]
27. Parra-Cabrera, C.; Achille, C.; Kuhn, S.; Ameloot, R. 3D printing in chemical engineering and catalytic technology: Structured catalysts, mixers and reactors. *Chem. Soc. Rev.* **2018**, *47*, 209–230. [[CrossRef](#)] [[PubMed](#)]
28. Reches, Y.; Livingston, J.; Ferguson, I.; Cranor, D.; Lobovsky, M.; Linder, N. Three-Dimensional Printer. US Patent Application No. 29/448,719, 3 February 2015.

29. Melnikova, R.; Ehrmann, A.; Finsterbusch, K. 3D printing of textile-based structures by Fused Deposition Modelling (FDM) with different polymer materials. In *IOP Conference Series: Materials Science and Engineering*; IOP Publishing: Bristol, UK, 2014; Volume 62, p. 012018.
30. Dixon, A.G. Correlations for wall and particle shape effects on fixed bed bulk voidage. *Can. J. Chem. Eng.* **1988**, *66*, 705–708. [[CrossRef](#)]
31. Jurtz, N.; Kraume, M.; Wehinger, G.D. Advances in Fixed-Bed Reactor Modeling using Particle-Resolved Computational Fluid Dynamics (CFD). *Rev. Chem. Eng.* **2019**, *35*, 139–190. [[CrossRef](#)]
32. Dixon, A.G.; Nijemeisland, M.; Stitt, E.H. Packed tubular reactor modeling and catalyst design using computational fluid dynamics. *Adv. Chem. Eng.* **2006**, *31*, 307–389.
33. Dixon, A.G.; Partopour, B. Computational Fluid Dynamics for Fixed Bed Reactor Design. *Annu. Rev. Chem. Biomol. Eng.* **2020**, *11*, 109–130. [[CrossRef](#)]
34. Eppinger, T.; Seidler, K.; Kraume, M. DEM-CFD simulations of fixed bed reactors with small tube to particle diameter ratios. *Chem. Eng. J.* **2011**, *166*, 324–331. [[CrossRef](#)]
35. Cundall, P.A.; Strack, O.D. A discrete numerical model for granular assemblies. *Geotechnique* **1979**, *29*, 47–65. [[CrossRef](#)]
36. Schiller, L. Über die grundlegenden Berechnungen bei der Schwerkraftaufbereitung. *Z. Vereines Dtsch. Inge.* **1933**, *77*, 318–321.
37. Eppinger, T.; Jurtz, N.; Aglave, R. Automated Workflow for Spatially Resolved Packed Bed Reactors With Spherical and Non-Spherical Particles. In Proceedings of the 10th International Conference on CFD in Oil & Gas, Metallurgical and Process Industries, SINTEF, Trondheim, Norway, 17–19 June 2014; pp. 1–10.
38. Wehinger, G.D.; Eppinger, T.; Kraume, M. Detailed numerical simulations of catalytic fixed-bed reactors: Heterogeneous dry reforming of methane. *Chem. Eng. Sci.* **2015**, *122*, 197–209. [[CrossRef](#)]
39. Wehinger, G.D.; Fütterer, C.; Kraume, M. Contact modifications for CFD simulations of fixed-bed reactors: Cylindrical particles. *Ind. Eng. Chem. Res.* **2016**, *56*, 87–99. [[CrossRef](#)]
40. Minhua, Z.; He, D.; Zhongfeng, G. A particle-resolved CFD model coupling reaction-diffusion inside fixed-bed reactor. *Adv. Powder Technol.* **2019**, *30*, 1226–1238. [[CrossRef](#)]
41. Wehinger, G.D. Particle-Resolved CFD Simulations of Catalytic Flow Reactors. Ph.D. Thesis, Technische Universitaet, Berlin, Germany, 2016.
42. Ergun, S. Fluid flow through packed columns. *Chem. Eng. Prog.* **1952**, *48*, 89–94.
43. Wakao, N.; Kagei, S. *Heat and Mass Transfer in Packed Beds*; Taylor & Francis: Abingdon, UK, 1982; Volume 1.
44. Yagi, S.; Kunii, D. Studies on effective thermal conductivities in packed beds. *AIChE J.* **1957**, *3*, 373–381. [[CrossRef](#)]
45. Dixon, A.G. Fixed bed catalytic reactor modelling—The radial heat transfer problem. *Can. J. Chem. Eng.* **2012**, *90*, 507–527. [[CrossRef](#)]
46. Wehinger, G.D.; Kraume, M.; Berg, V.; Korup, O.; Mette, K.; Schlögl, R.; Behrens, M.; Horn, R. Investigating dry reforming of methane with spatial reactor profiles and particle-resolved CFD simulations. *AIChE J.* **2016**, *62*, 4436–4452. [[CrossRef](#)]
47. Dong, Y.; Sosna, B.; Korup, O.; Rosowski, F.; Horn, R. Investigation of radial heat transfer in a fixed-bed reactor: CFD simulations and profile measurements. *Chem. Eng. J.* **2017**, *317*, 204–214. [[CrossRef](#)]

Publisher's Note: MDPI stays neutral with regard to jurisdictional claims in published maps and institutional affiliations.



© 2020 by the authors. Licensee MDPI, Basel, Switzerland. This article is an open access article distributed under the terms and conditions of the Creative Commons Attribution (CC BY) license (<http://creativecommons.org/licenses/by/4.0/>).